Numerical modeling of heat transfer and fluid flow in hybrid laser-TIG welding of aluminum alloy AA6082

Amir Hossein Faraji [a♣], Massoud Goodarzi [a], Seyed Hossein Seyedein [a], Giuseppe Barbieri [b] and Carmine Maletta [c]

[a] School of Metallurgy and Materials Engineering, Iran University of Science and Technology, Tehran, Iran.

[b] CR ENEA Casaccia, Rome, Italy.

[c] Department of Mechanical Engineering, University of Calabria, Arcavacata Rende, CS, Italy.

Abstract

This paper describes a 3D numerical model based on FVM (Finite Volume Method) to simulate heat transfer and fluid flow in laser-TIG hybrid welding process. A Gaussian surface heat source model is used for TIG heat input, and a new modified volumetric heat source model is presented for the laser heat input. Due to the presence of arc current, an appropriate electromagnetic model based on the Maxwell equations are also solved to calculate electromagnetic forces in the weld pool. A turbulence model based on Prandtl's mixing length hypothesis is used to take into account the presence of fluctuating velocities in the weld pool. The results of computer simulation, including temperature, current density, electromagnetic and melted material velocity field, are presented here. Furthermore, several dimensionless numbers are employed to recognize the importance of fluid flow driving forces in the weld pool. It is deduced that the fluid flow has an important effect on the weld pool shape. It is also founded that among the driving forces, Marangoni force is dominant fluid force in the weld pool. Besides, calculated results of hybrid welding process are compared with those of TIG and laser welding processes. The weld pool depth is relatively the same, but the width of the weld pool is highly larger in hybrid welding than lone laser welding. Eventually, the presented model is validated by comparison between calculated and experimental weld pool shape. It is founded that there is a good agreement as the capability of this model can be proved.

Keywords: Numerical modeling; heat transfer; fluid flow; weld pool; Hybrid welding; aluminum alloy.

♣ **Corresponding author:** Amir Hossein Faraji
Email: Amirhossein.faraji@gmail.com
Tel: +393895471233

1

1. Introduction

Hybrid laser-arc welding process is a new and modern welding process that is developing in many areas of industry including automotive, pipeline, aerospace and shipbuilding industry extremely fast because of its economical and technological advantages [1,2]. It is a process of joining two materials/workpieces using a laser and electrical arc to produce a structurally sound component [1,3,4]. Some reported advantages of hybrid laser-arc welding can be described as: more stable arc, more stable laser-generated keyhole, better process stability and efficiency, increase in the weld penetration depth and ability for welding in higher speed, compared to both lone arc and laser welding. As well, hybrid welding introduces better gap bridging ability, compared to lone laser welding, which can reduce machining costs and joint fitting difficulty. Finally, hybrid welding can improve the weld quality with reduced susceptibility to pores and cracks compared to lone laser welding process [4,1-3,5,6].

The benefits of hybrid welding arise due to synergy effect and interaction between two heat sources, i.e. laser and arc [1,7,3]. During laser and hybrid welding, a deep and narrow vapor filled cavity is created, the so-called keyhole, due to high-focused laser energy and thus allows for a much deeper weld penetration to be obtained [8,3,9]. Metal vapors leaving the laser generated keyhole is the main source of this laser-arc synergy when the arc and laser are in close proximity [3,5,1]. The high local vaporization rates of alloying elements leaving the keyhole produce a location of high electrical conductivity. Since the arc travels along the path with least electrical resistance, the arc tends to bend and root within close proximity of the keyhole [1-3]. In addition, the arc undergoes a contraction in which its radius decreases due to higher electrical conductivity of plasma in hybrid welding [3,10]. Both these phenomena result in increasing the arc stability, peak arc power density and then melting efficiency [3].

The shape and dimension of the weld pool is a key parameter in defining the weld strength [11-13]. The heat transfer and fluid flow in the weld pool has a strong effect on formation of the weld pool and then determination of the weld shape [12,14,15,3]. Molten metal circulation in the weld pool is mainly influenced by several driving forces including buoyancy, surface tension, and electromagnetic forces [12,16,17]. Numerical modeling has shown to be a successful tool for better understanding of temperature and velocity fields experienced in the weld pool [12,3,18,19].

Several experimental studies [20,21,6,22,7,10,5] have firmly proved the advantages of hybrid welding process. However, very few numerical studies are carried out on the hybrid welding process. W. Piekarska et al. [23,24] utilized a 3D mathematical model to estimate the temperature and velocity field for laser-arc hybrid welding. Fanrong Kong developed thermo-mechanical finite element model (FEM) considering only heat conduction to predict the temperature field and thermally induced residual stress in the hybrid laser-GMA welding process [25] and in hybrid laser-GTA welding of lap joint [26]. B. Ribic et al. [3] studied temperature fields, cooling rates and mixing in the weld pool of GTA-laser hybrid welding using a 3D numerical model. Zhiguo Gao et al. [27] calculated heat transfer and dynamic fluid flow in hybrid laser-arc welding of single-crystal nickel-base superalloys. G. X. Xu et al. [28] investigated thermal conduction mechanism in hybrid laser-pulsed GMA welding process of a mild steel. Emilie Le Guen et al. [29] extended a three-dimensional heat transfer model to predict the temperature fields and then the weld geometry during hybrid laser Nd:Yag-MAG arc welding of S355

steel. J. Zhou and H.L. Tsai [30] developed a mathematical model to investigate the complicated transport phenomena in spot hybrid laser-MIG keyhole welding of 304 stainless steel. Pei-quan Xu and et al. [31] simulated the heat transfer in laser–tungsten inert arc deep penetration welding between WC–Co cemented carbide and invar alloys.

To explain the main objective of this study, two points need to be mentioned. The first one is that in the majority of these studies, the effect of electromagnetic force in formation of the weld pool was not considered or just studied under axisymmetric condition. The second one is that almost all of previous numerical models developed in hybrid welding were related to steel alloys and modeling of the weld pool in aluminum alloy has received less attention in literatures. However, there is almost no numerical model developed to simulate the weld pool in hybrid laser-TIG welding of aluminum alloy AA6082.

In this study, a three-dimensional numerical model based on FVM (Finite Volume Method) is proposed to simulate heat transfer and fluid flow in the weld pool for laser-TIG hybrid welding of aluminum alloy AA6082. Since the problem is three-dimensional, an appropriate 3D electromagnetic model without assuming axisymmetric condition by solving four differential equations is used in this study. Besides, a new two-part volumetric heat source model for laser energy transferred to the material is incorporated into the proposed model. The mathematical formulation details of the model are, first, presented in sections 2. Then in section 3, the results of numerical modeling including the distribution of current density and electromagnetic forces, the temperature and velocity fields, the effect of liquid metal convection on the heat transfer, the role of individual driving forces, and the resulting pool geometry are described in detail. In addition, the comparison of weld pool shape and several weld characteristics among lone laser, lone TIG and hybrid welding are discussed in this section. Finally, the model was validated through comparison between calculated and experimental weld cross-sections.

Nomenclature

Φ scalar variable

Γ_Φ diffusion coefficient

S_Φ source term

x x coordinate (m)

y y coordinate (m)

z z coordinate (m)

u x-component of velocity (m.s^{-1})

v y-component of velocity (m.s^{-1})

w z-component of velocity (m.s^{-1})

ρ Density (Kg.m^{-3})

μ Viscosity (Kg.m^{-1}.s^{-1})

C_p Specific heat (J.kg^{-1}.K^{-1})

k Thermal conductivity (W.m^{-1}.K^{-1})

σ Electrical conductivity (Ω^{-1}.m^{-1})

β Thermal expansion coefficient (K^{-1})

T Temperature (K)

h Sensible heat enthalpy (J.kg^{-1})

P Pressure (Pa)

φ Electric potential (V)

g Acceleration of gravity (m.s^{-2})

T_{ref} Reference temperature (K)

ΔH Latent heat content (J.kg^{-1})

L_f Latent heat of fusion (J.kg^{-1})

f_l Liquid fraction

T_l Liquidus temperature (K)

T_s Solidus temperature (K)

C Mushy zone morphology constant (1.6×10^4)

μ_m Magnetic permeability ($4\pi\times10^{-7}\,N.A^{-2}$)

$\dfrac{d\gamma}{dT}$ Marangoni temperature coefficient (Kg.K^{-1}.s^{-2})

q_{conv} Convection heat loss (w.m^{-2})

$\vec{J}$ Current density vector (A.m^{-2})

$\vec{B}$ Magnetic field vector (kg.A^{-1}.s^{-2})

$\vec{A}$ potential vector (V)

$\vec{F}_{Lorentz}$ Electromagnetic force (N.m^{-3})

J_x x-component of current density (A.m^{-2})

J_y y-component of current density (A.m^{-2})

J_z z-component of current density (A.m^{-2})

B_x x component of magnetic field (kg.A^{-1}.s^{-2})

B_y y component of magnetic field (kg.A^{-1}.s^{-2})

B_z z component of magnetic field (kg.A^{-1}.s^{-2})

A_x x component of potential vector (V)

A_y y component of potential vector (V)

A_z z component of potential vector (V)

$F_{Lorentz}\big|_x$ x-component of Electromagnetic force (N.m^{-3})

$F_{Lorentz}\big|_y$ y-component of Electromagnetic force (N.m^{-3})

$F_{Lorentz}\big|_z$ z-component of Electromagnetic force (N.m^{-3})

Pr   Prandtl number

l_m Mixing length (m)

μ_l Laminar viscosity (Kg.m^{-1}.s^{-1})

μ_t Turbulent viscosity (Kg.m^{-1}.s^{-1})

$\mu_{effective}$ Effective viscosity (Kg.m^{-1}.s^{-1})

k_l Laminar thermal conductivity (W.m^{-1}.K^{-1})

k_t Turbulent thermal conductivity (W.m^{-1}.K^{-1})

$k_{effective}$ Effective thermal conductivity (W.m^{-1}.K^{-1})

r Radial distance from laser focal point (m)

I Current (A)

V Voltage (V)

η_{arc} Arc efficiency

R_{arc} Effective radius of arc (m)

f_{arc} Arc distribution parameter

q_{rad}	Radiation heat loss (w.m^{-2})	P_{laser}	Laser power (W)
h_f	Heat transfer coefficient (w.K^{-1}.m^{-2})	η_{laser}	Absorption coefficient of Laser beam
T_a	Ambient temperature (K)	R_{laser}	Effective radius of laser (m)
$\sigma_{Boltz.}$	Stefan-Boltzman constant	f_{laser}	Laser distribution parameter
ε	Surface emissivity	χ_{upper} , χ_{lower}	Laser energy factors
T_{max}	Maximum temperature (K)	r_e , r_i	Radius of cone ends (m)
$\left|\vec{V}\right|_{max}$	Maximum velocity (m.s^{-1})	z_i	z-coordinate of cone end (m)
Pe	Peclet number	$z_{keyhole}$	Keyhole depth (m)
Gr	Grashof number	V_w	Welding speed (m.s^{-1})
Rm	Magnetic Reynolds number	q_{arc}	Arc heat input (W.m^{-2})
Ma	Surface tension Reynolds number	J_{arc}	Arc current density (A.m^{-2})
$R_{M/B}$	Ratio of electromagnetic to Buoyancy force	q_{laser}	Laser heat input (W.m^{-3})
$R_{S/B}$	Ratio of surface tension to Buoyancy force	x_0	Initial x-position of heat source (m)
U	Characteristic velocity of molten metal (m.s^{-1})	L_B	Characteristic length for buoyancy force (m)
L_R	Characteristic length of weld pool (m)		

2. Numerical model

A schematic plot of calculation domain and boundary surfaces is demonstrated in Fig. 1. As seen, only half of the workpiece is considered because of the symmetry of the weld about the weld center line and a three dimension Cartesian coordinate system is used. In addition, Calculation domain has dimensions of 40 mm in length, 15 mm in width and 3 mm in depth.

Since the welding heat source moves with a certain velocity, thus the welding problem is unsteady when view from the stationary and fixed frame. But, in a coordinate system moving with the heat source, the problem can be modeled as a steady-state problem a short time after starting the welding.

In addition, to simplify the model, following assumptions are made in the model:

- The flow is Newtonian and incompressible with regard to the presence of a relatively small weld pool [3,14,18].
- The top surface is assumed to be flat. Instead, a volumetric heat source model for laser is applied to involve the effect of keyhole in the weld pool formation [24,31,32].
- The heat and current fluxes of the arc source have Gaussian distribution on the weld top surface.
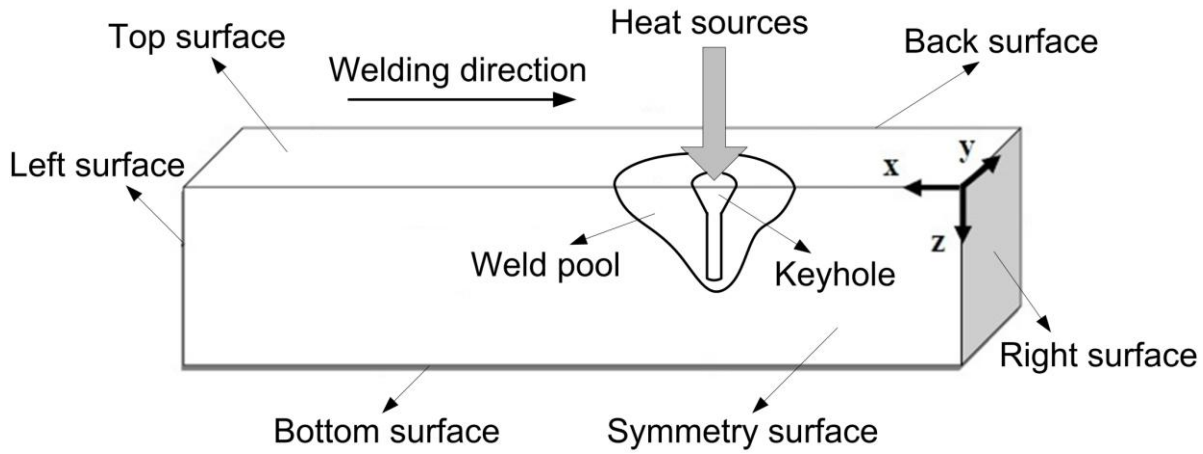
Fig. 1. Calculation domain and boundary surfaces used in the numerical model.

2.1. Governing equations

The steady-state general form of conservation equations proposed by Patankar [33], can be written as follows:

$$\vec{\nabla}.(\rho \vec{V} \Phi) = \vec{\nabla}.(\Gamma_\Phi \vec{\nabla} \Phi) + S_\Phi \tag{1}$$

The term on the left side of this equation represents transfer of variable by convection flux, the first term on the right side represents transfer of variable by diffusion flux and the second term is source term. In 3D Cartesian coordinate system, this general equation can be expressed as follow:

6

$$\frac{\partial(\rho u\Phi)}{\partial x}+\frac{\partial(\rho v\Phi)}{\partial y}+\frac{\partial(\rho w\Phi)}{\partial z}=\frac{\partial}{\partial x}\left(\Gamma_\Phi\frac{\partial\Phi}{\partial x}\right)+\frac{\partial}{\partial y}\left(\Gamma_\Phi\frac{\partial\Phi}{\partial y}\right)+\frac{\partial}{\partial z}\left(\Gamma_\Phi\frac{\partial\Phi}{\partial z}\right)+S_\Phi \qquad (2)$$

Φ, Γ_Φ and S_Φ are expressed for all solved conservation equations in table 1. As seen, nine differential equations are solved simultaneously in this numerical model. The last four equations, Eqs. (8)-(11), are solved to obtain the distribution of the current density, magnetic field and electromagnetic force in the workpiece.

The first source term in all x, y and z-momentum equations, Eqs. (4)-(6), is the pressure gradient, the second term is frictional dissipation in the mushy zone according to the Carman-Kozeny equation for flow through a porous media [19,34,9,18], the third term arises due to moving the welding heat source and the fourth term is the electromagnetic force in the weld pool. Where C is a constant related to the mushy zone morphology (set at 1.6×10^4 in this study [19,34,9,18]), and B is a very small constant introduced to avoid division by zero. The fifth term in right side of z-momentum equation is the buoyancy force in the weld pool. In the energy equation, Eq. (7), the first three terms are because of the melting of material, the next two terms are due to the motion of the welding heat source, the sixth term is Joule heating effect [17,11,12], and the last term is laser heat input to the workpice due to the keyhole formation.

2.2. Melting model

In the welding process, the material is melted because of heat input from welding heat sources. Hence, an appropriate melting model is needed to trace the weld pool solid-liquid interface. Accordingly, the total enthalpy, H, is defined by a sum of sensible heat, h, and latent heat content, ΔH, i.e. $H = h + \Delta H$ [3,18,19]. The latent heat content is calculated as follows:

$$\Delta H = f_l L_f \qquad (12)$$

The liquid fraction, f_l, is assumed to vary linearly with the temperature in the mushy zone for simplicity and is given as [19,35,11,12,36]:

$$f_l = \begin{cases} 0 & T < T_s \\ \dfrac{T-T_s}{T_l-T_s} & T_s \le T \le T_l \\ 1 & T > T_l \end{cases} \qquad (13)$$

Table 1. Conservation equations written in the form proposed by Patankar [33].

7

Conservation equation	Φ	Γ_φ	S_φ
Mass (Eq. (3))	1	0	0
x-momentum (Eq. (4))	u	μ	$-\dfrac{\partial p}{\partial x}-C\left(\dfrac{(1-f_l)^2}{f_l^3+B}\right)u-V_w\dfrac{\partial(\rho u)}{\partial x}+F_{Lorentz}\big|_x$
y-momentum (Eq. (5))	v	μ	$-\dfrac{\partial p}{\partial y}-C\left(\dfrac{(1-f_l)^2}{f_l^3+B}\right)v-V_w\dfrac{\partial(\rho v)}{\partial x}+F_{Lorentz}\big|_y$
z-momentum (Eq. (6))	w	μ	$-\dfrac{\partial p}{\partial z}-C\left(\dfrac{(1-f_l)^2}{f_l^3+B}\right)w-V_w\dfrac{\partial(\rho w)}{\partial x}+F_{Lorentz}\big|_z+\rho g\beta(T-T_{ref})$
Energy (Eq. (7))	h	$\dfrac{k}{C_p}$	$\dfrac{\partial(\rho u\Delta H)}{\partial x}-\dfrac{\partial(\rho v\Delta H)}{\partial y}-\dfrac{\partial(\rho w\Delta H)}{\partial z}-V_w\dfrac{\partial(\rho h)}{\partial x}-V_w\dfrac{\partial(\rho\Delta H)}{\partial x}$ $+\dfrac{J_x^2+J_y^2+J_z^2}{\sigma}+q_{laser}$
Electrical potential (Eq. (8))	φ	σ	0
x-vector potential (Eq. (9))	V_x	1	$\mu_m J_x$
y-vector potential (Eq. (10))	V_y	1	$\mu_m J_y$
z-vector potential (Eq. (11))	V_z	1	$\mu_m J_z$

2.3. Electromagnetic model

Due to the presence of an arc heat source in the hybrid welding process, an appropriate model must be used to consider the effect of the arc current and then electromagnetic force in the weld pool. Most previous studies either did not take into account this effect or assumed a 2D asymmetric model to calculate the current density and electromagnetic force in the cylindrical coordinates (r, z). However in this study, a particular 3D model without any assumption of axial symmetry is utilized to determine the distribution of current density, magnetic and electromagnetic force vectors in the workpiece.

The scalar potential is obtained by solving Eq. (8). Thereafter, current density components can be computed as follow [37-39]:

$$\vec{J}=-\sigma\vec{\nabla}\varphi\Rightarrow\begin{cases}J_x=-\sigma\dfrac{\partial\varphi}{\partial x}\\[2mm]J_y=-\sigma\dfrac{\partial\varphi}{\partial y}\\[2mm]J_z=-\sigma\dfrac{\partial\varphi}{\partial z}\end{cases}\tag{14}$$

8

The magnetic field self-induced by the arc is obtained by solving vector potential Eqs. (9)-(11) and then by means of the following formula [39,13]:

$$\vec{B} = \vec{\nabla} \times \vec{A} \Rightarrow \begin{cases} B_x = \dfrac{\partial A_z}{\partial y} - \dfrac{\partial A_y}{\partial z} \\[2mm] B_y = \dfrac{\partial A_x}{\partial z} - \dfrac{\partial A_z}{\partial x} \\[2mm] B_z = \dfrac{\partial A_y}{\partial x} - \dfrac{\partial A_x}{\partial y} \end{cases} \tag{15}$$

Eventually, the electromagnetic Lorentz force vector can be calculated through the following equation [39,16,14]:

$$\vec{F}_{Lorentz} = \vec{J} \times \vec{B} \Rightarrow \begin{cases} F_{Lorentz}\big|_x = J \times B\big|_x = J_y\,B_z - J_z\,B_y \\[2mm] F_{Lorentz}\big|_y = J \times B\big|_y = J_z\,B_x - J_x\,B_z \\[2mm] F_{Lorentz}\big|_z = J \times B\big|_z = J_x\,B_y - J_y\,B_x \end{cases} \tag{16}$$

2.4. Turbulence model

During welding, due to the presence of fluctuating velocities in the weld pool, the rates of the transport of heat, mass and momentum are mostly increased. These phenomena should be considered by an appropriate turbulence model that presents an approach to calculate effective viscosity and thermal conductivity in the melted weld pool. In this study, a turbulence model based on Prandtl's mixing length hypothesis presented in previous literatures [18,3,9] is used to calculate the turbulent viscosity.

$$\mu_t = 0.3 \rho l_m V \tag{17}$$

Where l_m is the mixing length and is taken as the nearest distance from the weld pool boundary. The corresponding turbulent thermal conductivity is defined from the turbulent Prandtl number as the following relationship:

$$\mathrm{Pr} = \frac{\mu_t C_p}{k_t} \tag{18}$$

Here, the turbulent Prandtl number is set to a value of 0.9. Finally, the effective viscosity and thermal conductivity can be calculated as the sum of the turbulent and laminar parts [18,3,9], given as follows:

$$\begin{cases} \mu_{effective} = \mu_l + \mu_t \\ k_{effective} = k_l + k_t \end{cases} \tag{19}$$

9

2.5. Heat source model

Heat transfer and fluid flow in the weld pool are extremely affected by the distribution of heat input entered to the workpiece by the welding heat sources. Since the characteristics of laser and arc heat sources are completely different in hybrid welding process, two different heat source power distribution models should be used. Accordingly, a surface heat source model is used for TIG power distribution and a volumetric heat source model is used for laser power distribution. These heat sources are explained in detaied below.

2.5.1. TIG heat source model

Since the arc heat is mostly entered to workpiece from the top surface, a Gaussian surface heat source model is used for heat input from TIG source in this study. In addition, a Gaussian current density flux is also considered here.

$$q_{arc} = \frac{\eta_{arc} f_{arc} VI}{\pi R_{arc}^2} \exp(-\frac{f_{arc} r^2}{R_{arc}^2}) \tag{20}$$

$$J_{arc} = \frac{f_{arc} I}{\pi R_{arc}^2} \exp(-\frac{f_{arc} r^2}{R_{arc}^2}) \tag{21}$$

Where r is radial distance to the arc rout and can be written as $r = \sqrt{(x-x_0)^2 + y^2}$.

2.5.2. Laser heat source model

In hybrid welding, high laser power creates a cavity containing ionized vapors named keyhole [10,3,30]. Several physical absorption mechanisms by the walls of formed keyhole cause to transport of the laser energy below the surface of the workpiece [3,31]. So, based on the reversed-bugle shape of the laser-created keyhole [30], a combined effective heat source model is applied in this study. It consists of a conical volumetric heat source at the upper part and a cylindrical volumetric heat source at the lower part, as schematically demonstrated in Fig. 2.

Upper part

For $0 < z < z_i$:

$$
\begin{cases}
q_{laser} = \dfrac{\chi_{upper}\,\eta_{laser}\,f_{laser}^2\,P_{laser}}{\pi(1-e^{-3})\,(z_i)\,(r_i^2 + r_i.r_e + r_e^2)}\exp(-\dfrac{f_{laser}\,r^2}{R_{laser}^2}) \\[4mm]
r = \sqrt{(x-x_0)^2 + y^2} \\[4mm]
R_{laser} = r_i + \dfrac{(r_i - r_e)}{z_i}.(z - z_i)
\end{cases}
\qquad (22)
$$

Lower part

For $z_i < z < z_{keyhole}$:

$$
q_{laser} = \frac{\chi_{lower}\,\eta_{laser}\,P_{laser}}{\pi r_i^2\,(z_{keyhole} - z_i)}
\qquad (23)
$$

Where $\chi_{upper} + \chi_{lower} = 1$.
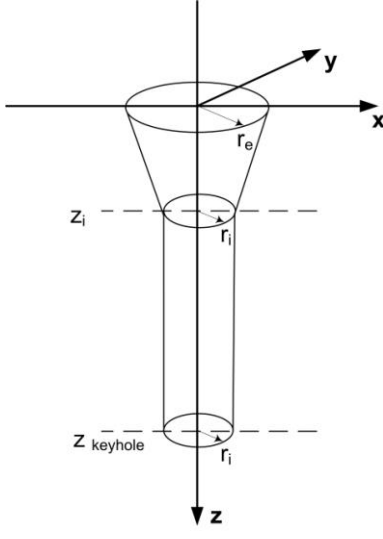
Fig. 2. Schematic presentation of volumetric model of the laser heat source used in modeling.

2.6. Boundary conditions

The boundary conditions used in present model are indexed in table 2. At the top surface, Marangoni stress arisen from temperature gradient of surface tension coefficient is exerted for momentum equations. For energy equation, arc heat input minus convective and radiation heat loss is considered

11

and the arc current density flux is considered for the potential equation. The heat loss due to convection (q_{conv}) and radiation (q_{rad}) can be expressed as:

$$\begin{cases} q_{conv} = h_f\,(T-T_a) \\ q_{rad} = \sigma_{Boltz.}\,\varepsilon\,(T^4 - T_a^4) \end{cases} \tag{24}$$

At the symmetry surface, symmetric condition is applied for all dependent variables. At the bottom surface, since the weld pool does not extend to the bottom and only partial weld penetration is considered here, all velocities are set at zero, and heat loss by the convection and radiation are used for energy equation. At the other surfaces far away from the heat sources, the temperature is set at ambient temperature and the velocities are set to be zero.

Table 2. Boundary conditions used in the numerical model.

	u	v	w	T	φ	V_X	V_y	V_z
Top surface	$\mu\dfrac{\partial u}{\partial z} = f_l\dfrac{d\gamma}{dT}\dfrac{\partial T}{\partial x}$	$\mu\dfrac{\partial v}{\partial z} = f_l\dfrac{d\gamma}{dT}\dfrac{\partial T}{\partial y}$	$w=0$	$q = q_{arc} - q_{conv} - q_{rad}$	$J = J_{arc}$	$\dfrac{\partial V_x}{\partial z}=0$	$\dfrac{\partial V_y}{\partial z}=0$	$\dfrac{\partial V_z}{\partial z}=0$
Bottom surface	0	0	0	$q = q_{conv} + q_{rad}$	$\dfrac{\partial \varphi}{\partial z}=0$	$\dfrac{\partial V_x}{\partial z}=0$	$\dfrac{\partial V_y}{\partial z}=0$	$\dfrac{\partial V_z}{\partial z}=0$
Symmetry surface	$\dfrac{\partial u}{\partial y}=0$	0	$\dfrac{\partial w}{\partial y}=0$	$\dfrac{\partial T}{\partial y}=0$	$\dfrac{\partial \varphi}{\partial y}=0$	$\dfrac{\partial V_x}{\partial y}=0$	$\dfrac{\partial V_y}{\partial y}=0$	$\dfrac{\partial V_z}{\partial y}=0$
Back surfaces	0	0	0	$300\ \mathrm{K}$	$\varphi=0$	$\dfrac{\partial V_x}{\partial y}=0$	$\dfrac{\partial V_y}{\partial y}=0$	$\dfrac{\partial V_z}{\partial y}=0$
Left surface	0	0	0	$300\ \mathrm{K}$	$\varphi=0$	$\dfrac{\partial V_x}{\partial x}=0$	$\dfrac{\partial V_y}{\partial x}=0$	$\dfrac{\partial V_z}{\partial x}=0$
Right surface	0	0	0	$300\ \mathrm{K}$	$\varphi=0$	$\dfrac{\partial V_x}{\partial x}=0$	$\dfrac{\partial V_y}{\partial x}=0$	$\dfrac{\partial V_z}{\partial x}=0$

2.7. Numerical approach

In order to numerically solve the governing equations, FLUENT software is used. To enhance the FLUENT code for solving four additional equations taken from Maxwell equations, computing the

12

current density, magnetic field and electromagnetic force and also handling source terms and boundary conditions, particular abilities of FLUENT for adding C++ programming codes by UDF (User-Defined Function) and adding extra scalar equations by UDS (User-Defined Scalar) are used.

All governing equations are discretized based on FVM, where the calculation domain is divided into small hexahedral control volumes. A scalar grid point is located at the center of each cell storing the values of scalar quantities. A non-uniform fixed-grid configuration with finer grids near the heat source location is used. The total number of grid points used is 855000 chosen by convergence analysis, i.e. obtaining a good accuracy with low computational time. The standard SIMPLE (Semi-Implicit Method for Pressure-Linked Equation) algorithm is used for the pressure-velocity coupling and upwind scheme is used for discretization of the convection terms in the governing equations. To obtain convergence, the calculations were performed by applying the appropriate under-relaxation factor. The convergence of the calculations is reached when residual is less than defined convergence criteria. In the present study, the convergence criteria for momentum equations are defined to be 10^{-3} and that for other equations are set at 10^{-6}. The material properties employed for computation of heat transfer and fluid flow are listed in table 3.

Table 3. Material properties used in numerical model.

Property	symbol	Unit	Value
Density	ρ	Kg.m^{-3}	2700
Viscosity	μ	Kg.m^{-1}.s^{-1}	0.001
Thermal conductivity	k	W.m^{-1}.K^{-1}	$\begin{cases} 220 & ,T \leq 923 \\ 150 & ,T > 923 \end{cases}$
Specific heat	C_p	J.kg^{-1}.K^{-1}	$\begin{cases} 900 & ,T \leq 923 \\ 1200 & ,T > 923 \end{cases}$
Latent heat of fusion	L_f	J.kg^{-1}	395000
Thermal expansion	β	K^{-1}	2.3×10^{-5}
Liquidus temperature	T_l	K	923
Solidus temperature	T_s	K	858
Electrical conductivity	σ	A.V^{-1}.m^{-1}	3.12×10^7

3. Results and discussion

13

3.1. Heat source model adjustment

One of the most important parts in numerical modeling of the welding process is the adjustment of heat source parameters, i.e. the physical and phenomenological parameters reported in Eqs. (20) and (21) for the TIG source and in Eqs. (22) and (23) for the laser source.

In this study, the arc current and laser power are fixed at 100 A and 2000 W, respectively. The arc voltage which was taken from TIG machine is equal to about 15 V.

Arc heat source parameters consist of the arc energy efficiency (η_{arc}), arc distribution parameter (f_{arc}) and effective radius of the arc (R_{arc}). The arc distribution parameter determines the nature of the Gaussian heat distribution pattern which is set at 2 based on previous studies [40,41]. The arc energy efficiency depending on the arc stability is reported to be in the range of 65% to 85% [42,43]. Since the arc in hybrid welding process has usually high stability, the arc energy efficiency is assumed as 80% in this study. Therefore, the only parameter that should be adjusted in Eqs. (20) and (21) is the effective radius of the arc which is chosen as 1.5 mm in present model. It seems necessary to mention that the effective radius of the arc in lone TIG welding for 100 A arc with the arc length of 2 mm is reported to be about 2.5 mm [12,44,43]. However in hybrid welding, this parameter was set at 1.5 mm since in the hybrid welding, the arc is constricted because of the laser-arc interaction.

Laser heat source parameters consist of the laser absorption efficiency (η_{laser}), laser distribution parameter (f_{laser}), upper and lower laser energy factors (χ_{upper}, χ_{lower}), Radius of cone ends (R_i, R_e), z-coordinate of cone end (Z_i) and keyhole depth ($z_{keyhole}$).

Since presence of keyhole during hybrid welding results in a higher laser energy absorption by multiple internal reflections [30,3,27], the laser absorption efficiency is assumed to be 85%. Because of more focused heat distribution of laser than arc source and based on previous studies [3,18,19], the laser distribution parameter is taken as 3.

Based on predicted keyhole shapes reported in the previous literatures [30,45], the z-coordinate of cone end and Radius of cone ends were assumed as $Z_i = 0.25 Z_{keyhole}$ and $R_i = R_{laser}$, $R_e = 2R_{laser}$. As well, the upper and lower laser energy factors were set at 0.5.

Therefore, the only parameter that should be adjusted in Eqs. (22) and (23) is the keyhole depth which is chosen as 1.8 mm in our model.

In addition, because of the interaction between the arc and laser in hybrid welding and then bending the arc towards the keyhole, it is assumed that both the laser and arc sources are acting at the same location. Consequently, we set $x_0 = 15 \, mm$ in both laser and arc heat source equations.

The heat flux distribution of arc heat source on the top surface is illustrated in Fig. 3. Volumetric heat distribution of the laser heat source in longitudinal-section and top surface of the workpiece is demonstrated in Fig. 4.

14
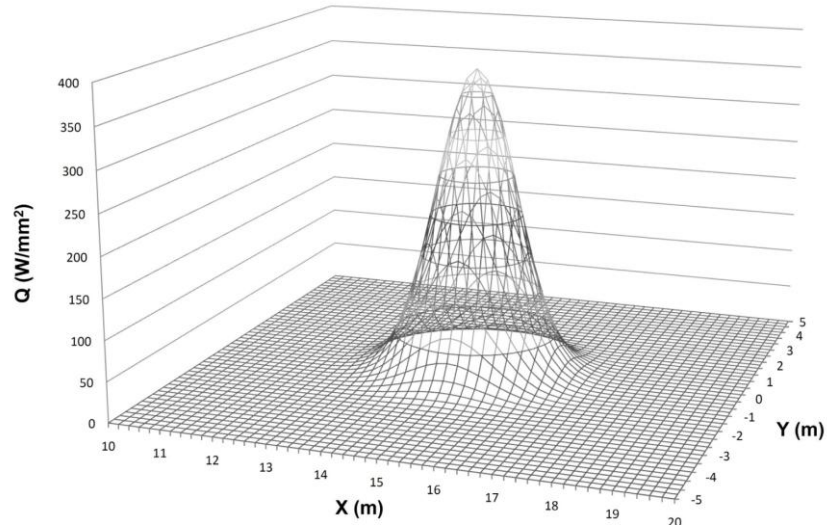
Fig. 3. Heat input distribution of the TIG source on the top surface.
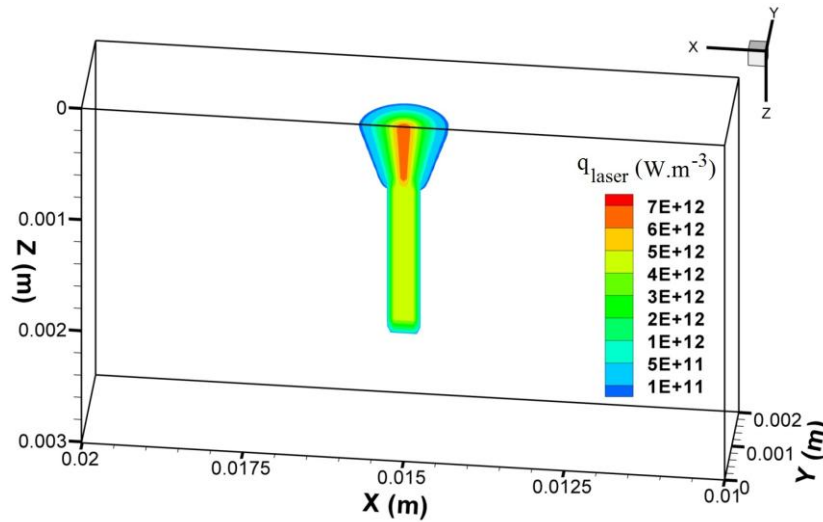
Fig. 4. Volumetric heat distribution of the laser source in the calculation domain.

3.2. Results of electromagnetic model

Fig. 5 shows the distribution of current density vectors in cross sectional surface of the weld. As seen, the current density attains its greatest value at the center position of the weld pool surface where the arc is concentrated above.

Fig. 6 shows the distribution of self-induced magnetic field at top surface of the weld. As shown, the magnetic field vectors mainly consist of the angular component especially in close vicinity of the arc axis that the magnetic field magnitude is higher.

15

Fig. 7 shows the electromagnetic (Lorentz) force vectors in the transverse weld cross section. As observed, Lorentz force causes inward and downward force and accordingly pulls the liquid metal along the surface towards the center and pushes it down to the bottom of the weld pool.

The variations of the current density, self induce magnetic field and Lorentz force along the y direction at the top surface and x=0.015 m is demonstrated in Fig. 8. As seen, the current density decreases continuously along the y direction. However, the magnetic field increases first to a maximum value and then decreases severely. Consequently, the distribution of the Lorentz force along the y direction shows a variation trend similar to the magnetic field.
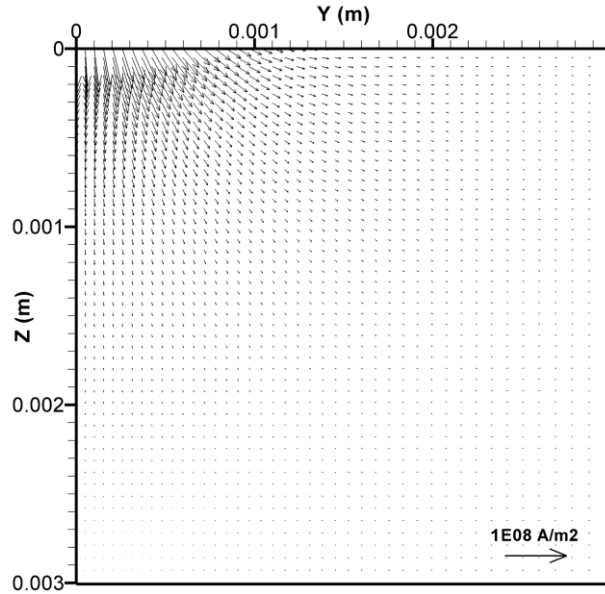
Fig. 5. Distribution of current density vectors in the transverse weld cross section.
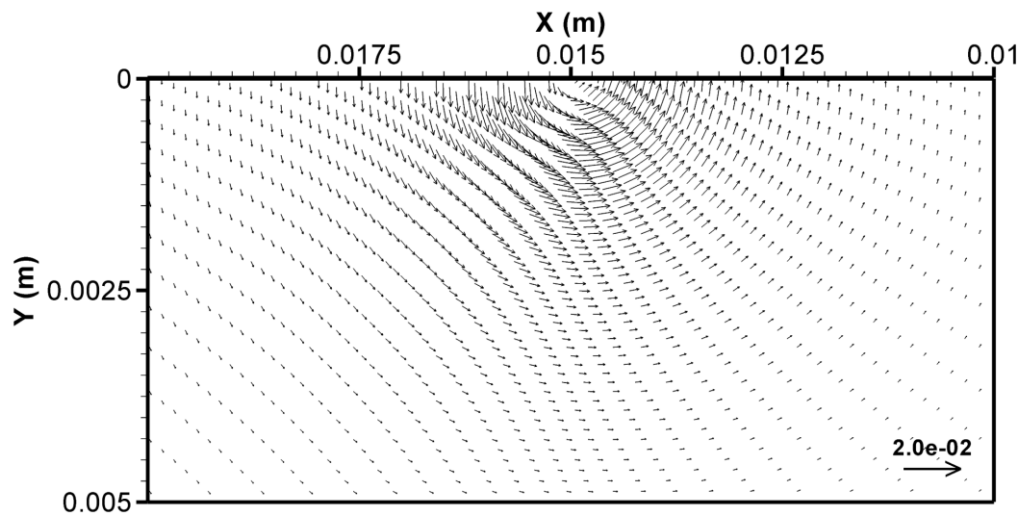
Fig. 6. Distribution of the magnetic field vectors at the top surface.
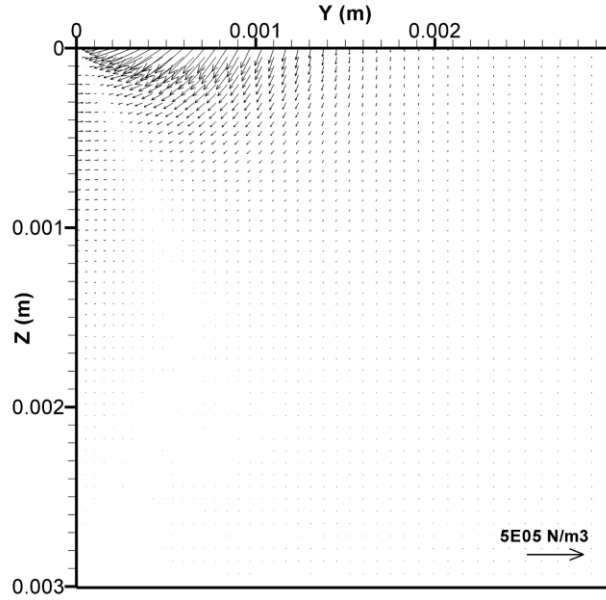
Fig. 7. Distribution of electromagnetic force vectors in the transverse weld cross section.
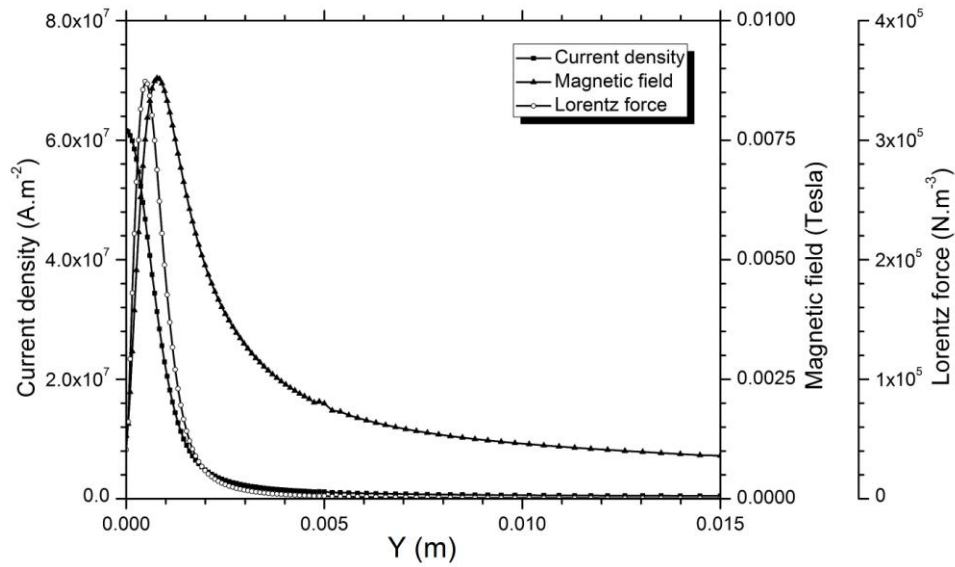
Fig. 8. Variations of the current density, magnetic field and Lorentz force along the y direction at the top surface and x=0.015 m.

3.3. Calculated temperature and velocity fields

Figs. 9-11 show the temperature contour plot and also fluid flow in the transverse cross section, longitudinal and top surface of the weld pool. As clearly seen in Fig. 11, the melted material at the top surface moves outward as tends to widen the weld pool because of the powerful Marangoni force. In addition, it can be found from Fig. 9 that there is a circulation loop of fluid near the top surface. Both of these events can prove the significant effect of the Marangoni force in the weld pool. The other fact understood from Figs. 10 and 11 is that the weld pool bulge towards the rear along the welding direction, which is caused by moving heat source of welding.

Fig. 12 demonstrates the variation of the temperature along the x direction on the top surface at different y locations. As seen, all plots have a maximum point at the position under the heat source location. As well, the maximum temperature decreases with moving further away from the weld centerline.

Fig. 13 shows the variation of the temperature and velocity along the y direction at the top surface of workpiece. As seen, the maximum temperature and velocity experienced in the weld pool are about 3500 K and 0.55 m.s^{-1}, respectively. The velocity of fluid material in the weld pool increases first sharply and after reaching a maximum decreases rapidly to zero. But the temperature changes continuously along the y direction reaching to the ambient temperature. Besides, the temperature reaches the ambient temperature at the distance of approximately 5 mm, which it means that the side walls of workpiece are far enough to not be affected by heating of the welding sources.
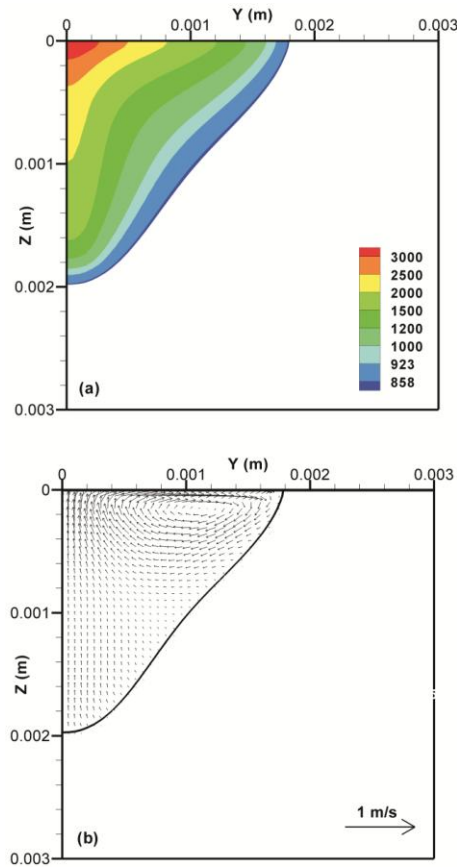
Fig. 9. (a) Temperature contours and (b) velocity field in transverse weld cross section.

18
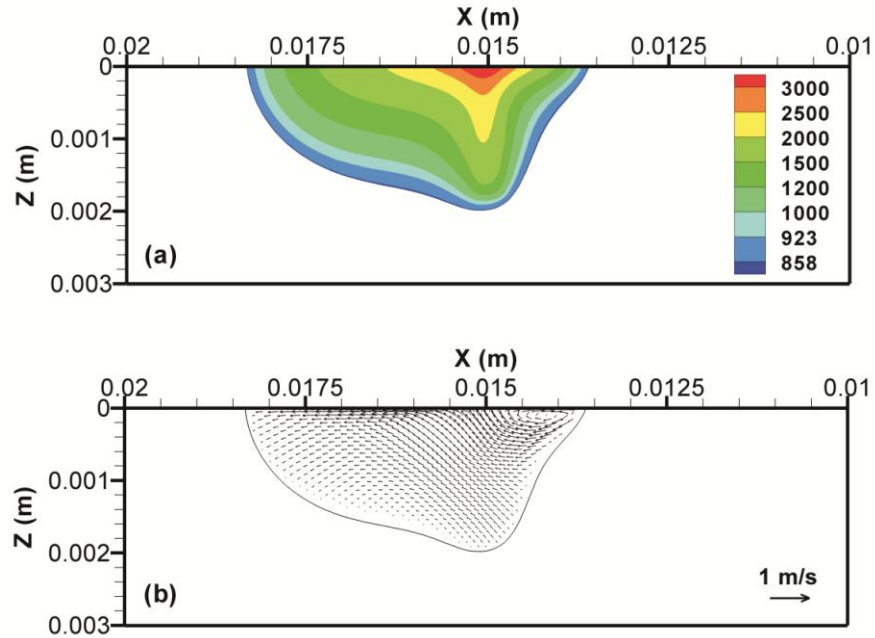
Fig. 10. (a) Temperature contours and (b) velocity field in the weld pool in the longitudinal section.
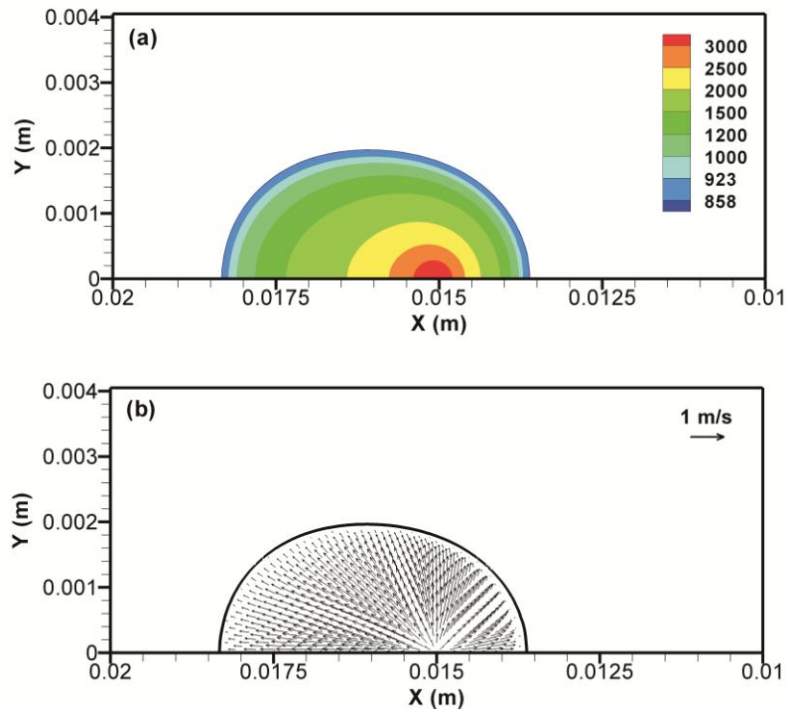
Fig. 11. (a) Temperature contours and (b) velocity field in the weld pool at the top surface.
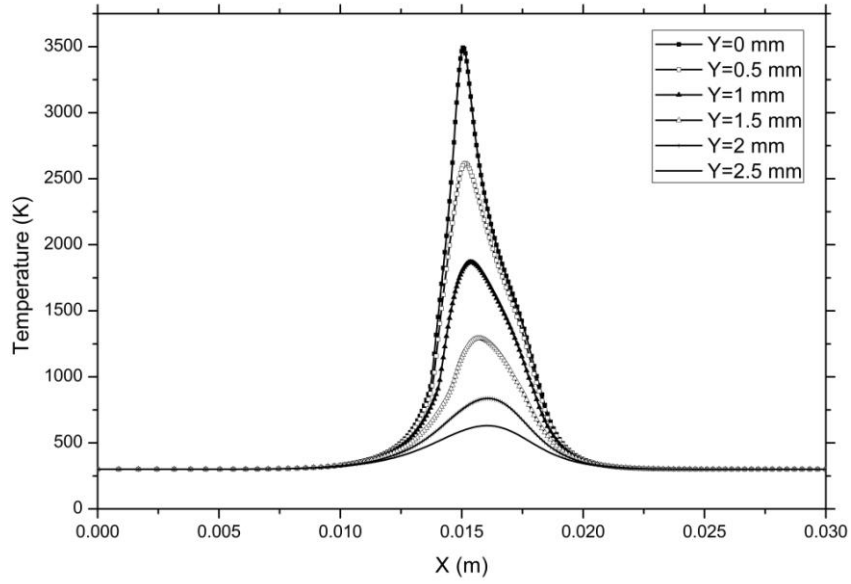
Fig. 12. Variation of the temperature along the x direction at the top surface and at different y locations.
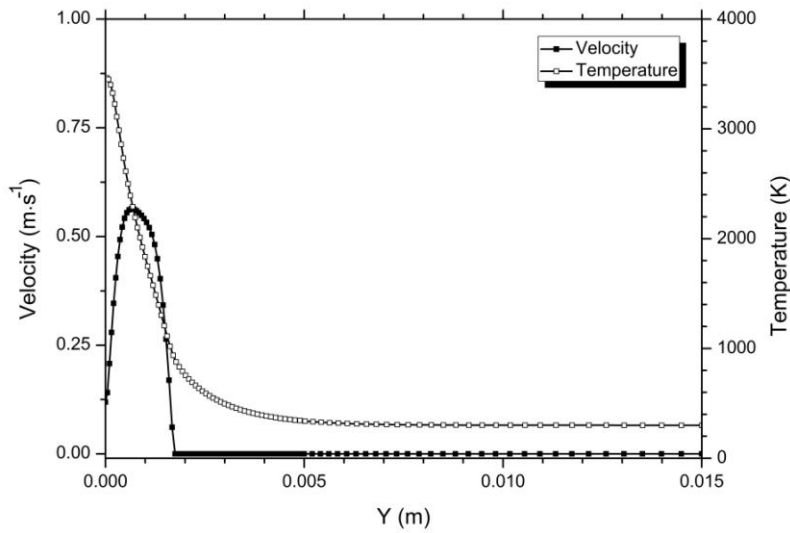
Fig. 13. Variations of the temperature and velocity along the y direction at the top surface and x=0.015 m.

3.4. The effects of driving forces

Several characteristic parameters of the weld pool calculated for various cases are summarized in table 4. As shown, the maximum temperature for the case without considering convection (considering only conduction) is higher than that for the case considering all driving forces. The higher calculated maximum temperature in the absence of convection is because the fluid flow plays an effective role in dissipating heat in the weld pool. In addition, velocity values in the case of Marangoni stress are higher relative to two other cases, i.e. buoyancy and electromagnetic forces. It means that the Marangoni convection cause a faster circulation in the weld pool than other driving forces. In order to estimate the relative influence of each heat transfer mechanism on the weld pool dimensions, the depth and half width of the weld pool are also summarized in this table for each case. As observed, the width of the weld pool is lower in the case without considering convection than the case with considering convection. This is because the Marangoni force, as a strong driving force, pushes melted material outwards on the weld pool surface and thus widens the weld pool.

Fig. 14 demonstrates the comparison of calculated transverse weld cross section for two cases, with and without considering convection, with experimental one. As seen, the calculated weld pool shape at the presence of convection is closer to experimental weld shape. It means that to predict the weld pool shape more precisely, it is necessary to take into account both heat transfer mechanisms, i.e. conduction and convection, in numerical modeling.

Table. 4. Effect of different driving forces on the weld pool characteristics in hybrid welding.

	T_{max} (K)	u_{max} (m/s)	v_{max} (m/s)	w_{max} (m/s)	Depth (mm)	Half width (mm)
Only conduction	4417	0	0	0	1.88	1.4
Marangoni stress	3464	0.657	0.577	0.139	1.98	1.78
Buoyancy force	4196	0.227	0.05	0.048	2.02	1.62
Electromagnetic force	4200	0.22	0.05	0.047	2.01	1.61
All driving forces	3492	0.645	0.566	0.137	1.99	1.8
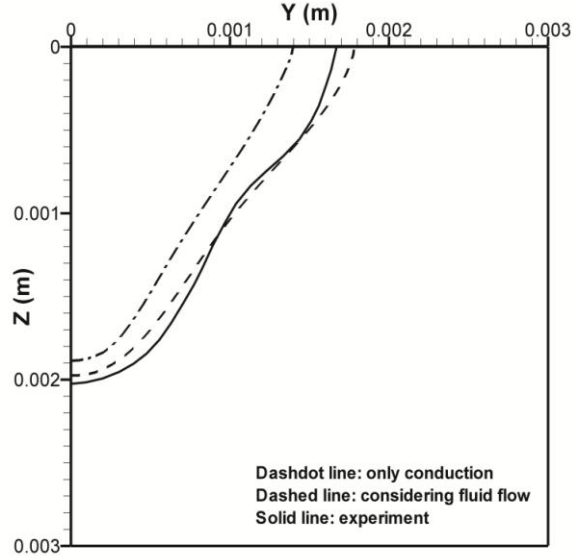
Fig. 14. Comparison of the experimental weld pool shape with calculated one for two cases, with and without considering convection, for hybrid welding process.

The effects of heat conduction and convection and also each driving force on the weld pool can be evaluated by using several dimensionless numbers. The dimensionless Peclet number is used to evaluate the relative significance of heat transfer by convection relative to conduction in weld pool, which is given as [18,35,16]:

$$Pe = \frac{Convective}{Conduction} = \frac{\rho C_p U L_R}{k} \tag{25}$$

Where U is taken as the maximum velocity experienced in the weld pool and L_R is taken as the half width of the weld pool.

The driving forces for fluid flow in the weld pool, considered in this study, include the surface tension, buoyancy and electromagnetic forces. To estimate the relative importance of each driving force, several dimensionless numbers are used in present study.

Grashof number determines the ratio of buoyancy force to viscous force and is calculated by [16,46,3]:

$$Gr = \frac{\beta g \rho^2 L_B^3 \Delta T}{\mu^2} \tag{26}$$

Where L_B is taken as one eighth of the weld pool width and ΔT is temperature difference between the maximum temperature in the weld pool and the solidus temperature, i.e. $\Delta T = T_{max} - T_s$.

Surface tension Reynolds number determines the ratio of surface tension (Marangoni) force to viscous force and is given by [16,46,3]:

$$Ma = \frac{\rho^2 L_R \Delta T \left|\frac{\partial \gamma}{\partial T}\right|}{\mu^2} \qquad (27)$$

Electromagnetic Reynolds number defines the ratio of electromagnetic (Lorentz) force to viscous force and is given as [16,46,3]:

$$Rm = \frac{\rho \mu_m I^2}{4\pi^2 \mu^2} \qquad (28)$$

The relative significance of these driving forces can be judged using the combination of these dimensionless numbers. The ratio of Marangoni force to buoyancy force is determined by $R_{S/B} = Ma/Gr$ and the ratio of Lorentz force to buoyancy force is determined by $R_{M/B} = Rm/Gr$.

Based on the results listed in table 4 and the equations explained above, Pe, Gr, Ma and Rm in hybrid welding are defined to be 23.8, 394.4, 8.6×10^5 and 1.9×10^6, respectively. Since calculated Peclet number is much greater than one, it means that the heat is mainly transferred by convection compared to conduction and, consequently, the fluid flow in the weld pool noticeably affects the weld pool shape. In addition, it can be predicted that the fluid flow is mostly driven by the Marangoni and electromagnetic forces and, to a much less extent, by the buoyancy force. Besides, the Marangoni force is the dominant driving force for heat convection in the weld pool in hybrid welding process.

3.5. Comparison of hybrid welding with laser and TIG welding

Fig. 15 shows comparison of the weld pool shape among TIG, laser and hybrid welding processes. The weld pool in TIG welding is shallow and wide, but in laser welding, it is reversely deep and narrow. As well, the geometry of hybrid weld is a combination of that of the laser and arc welds. It means that the arc heat merely melts the surface of the base metal and does not deepen the penetration and the laser deepens the weld pool. In addition, the weld width in hybrid welding is larger than that of lone TIG and laser welding. There are two reasons for this fact, one is larger volume of melted material generated by two heat sources and the other is stronger Marangoni stress in hybrid welding than lone arc and laser welding.

Fig 16 and 17 show the variation of the temperature along the x and y direction at the top surface for lone laser and hybrid welding. As expected, the peak temperature is higher and as well, the distribution of the temperature is wider in case of hybrid welding than lone laser welding.

The distribution of the velocity along the y direction at top surface for both laser and hybrid welding is plotted in Fig. 18. As seen, the maximum velocities are almost of the same order, but the velocity distribution is wider for hybrid welding than lone laser welding.
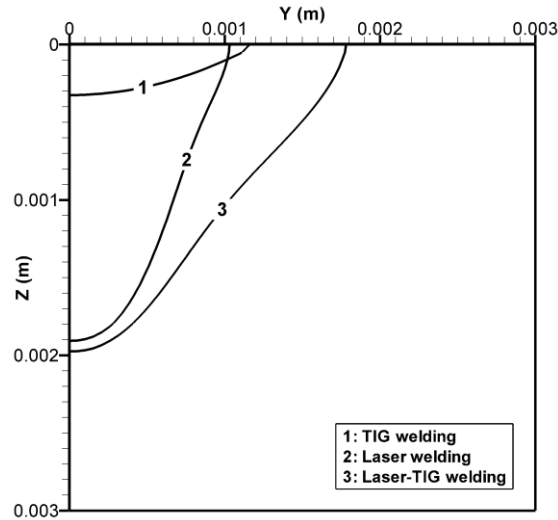
Fig. 15. Comparison of weld pool cross-sectional geometry among TIG, laser and hybrid welding processes.
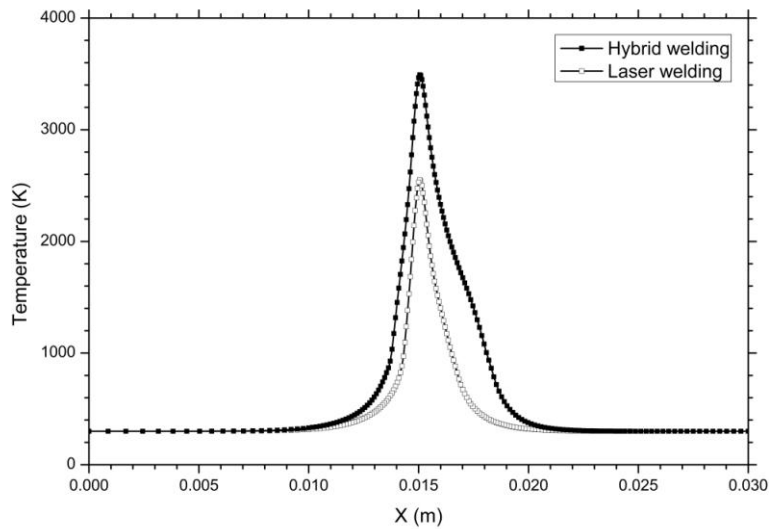
Fig. 16. Comparison of calculated temperature distribution along the x direction between laser and hybrid welding processes.
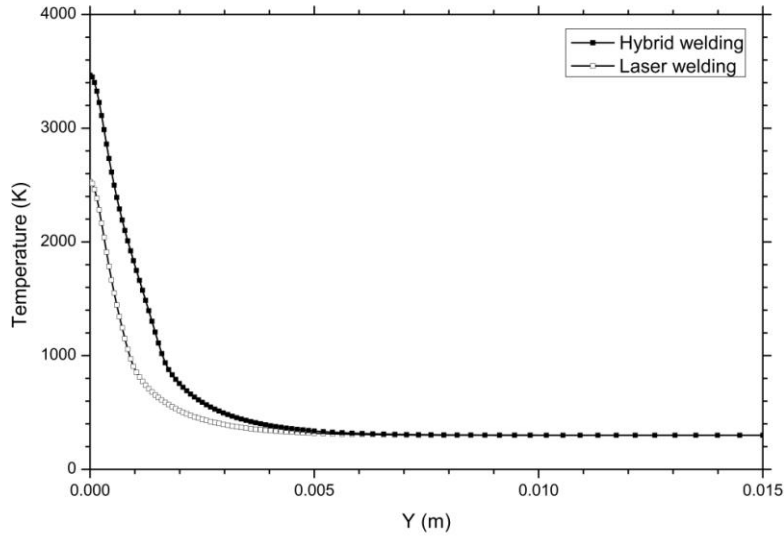
Fig. 17. Comparison of calculated temperature distribution along the y direction between laser and hybrid welding processes.
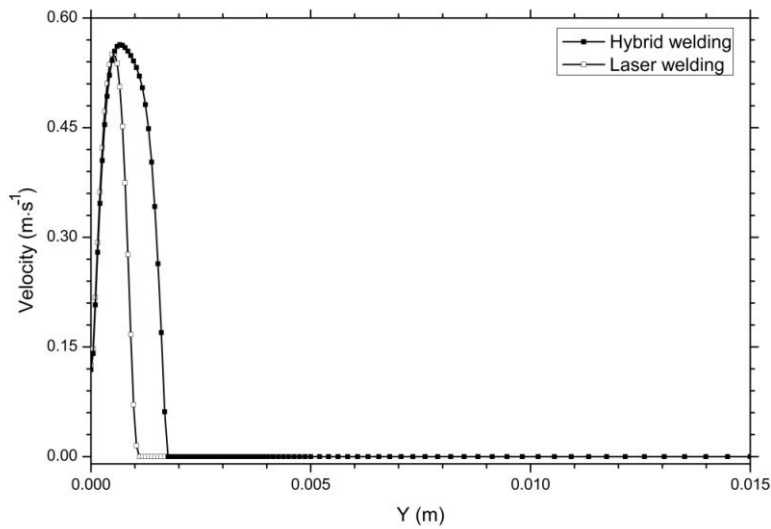
Fig. 18. Comparison of calculated velocity distribution along the y direction between laser and hybrid welding processes.

25

Several characteristics of the weld pool for all three welding processes, i.e. lone TIG, lone laser and hybrid welding are compared in table 5. As seen, the maximum temperature is the highest in case of hybrid welding and, also, the maximum temperature is higher for laser welding than TIG welding case. The reason can be explained by the amount of heat input from the welding heat source. The heat input is the greatest in hybrid welding case and, moreover, in laser welding is greater than TIG welding case. The maximum velocity in weld pool is almost the same for laser and hybrid welding cases. However, it is lower in case of lone TIG welding, which is probably attributed to weaker fluid flow forces in the weld pool. The dimensionless numbers for all three welding processes are also listed in this table. As seen, the Peclet number for all three cases is much higher than one, especially, in hybrid welding process. As well, the values of dimensionless numbers are greater in case of hybrid welding than lone laser or TIG welding process. Both of these facts confirm that the heat convection and fluid flow forces is more effective in the hybrid welding than the lone TIG or laser welding. In addition, based on the values summarized in this table, it can be also predicted that in all three cases, the fluid flow is mainly driven by the Marangoni and electromagnetic forces and, to a much less extent, by the buoyancy force.

Table. 5. Comparison of weld pool characteristics and Dimensionless numbers among TIG, laser and hybrid welding processes.

Variable	TIG welding	Laser welding	Hybrid welding
T_{max} (K)	1225	2552	3492
$\left\|\vec{V}\right\|_{max}$ (m/s)	0.443	0.615	0.612
Depth (mm)	0.33	1.9	1.98
Half width (mm)	1.15	1.02	1.8
Pe	11	13.6	23.8
Gr	14.3	46.2	394.4
Rm	8.6×10^5	-	8.6×10^5
Ma	1.7×10^5	6.9×10^5	1.9×10^6
$R_{M/B}$	6×10^4	-	2.2×10^3
$R_{S/B}$	1.2×10^4	1.5×10^4	4.8×10^3

3.6 Experiments and model validation

In order to validate the model, some experiments were carried out by using a Nd:YAG laser with maximum power of 2000 W accompanying by a TIG welder with maximum arc current of 350 A. The arrangement of laser and TIG torch is shown in Fig. 19. As clearly shown in this figure, laser-leading configuration, where the TIG torch is positioned prior to the laser along the welding direction, is used in this study. The laser power and arc current were set to be 2000 W, 100 A, respectively. Besides, two welding speeds of 2 and 3 m/min were used. The arc-to-laser distance, OX, and the arc length, OY, were taken as 0 and 2 mm, respectively. These values were chosen based on preliminary welding tests. The arc voltage was about 15 V. Spot diameter of the laser beam on the surface of the workpiece was about 0.5 mm. Argon was applied as the shielding gas. The inclination angle of the laser beam was 5°, and the angle between the weld torch and workpiece surface was 60°.

Before welding, each specimen was sanded by steel wire brush and degreased with acetone to remove oxides and other residue. Thereafter, hybrid linear bead-on-plate welds were made on the plate of AA6082 aluminum alloy with the thickness of 3 mm.

For the sake of comparison between numerical predictions and experiments, the shape and dimensions of the weld pool were measured by optic microscopic observations. For this aim, specimens were cut from welded sheets and then mounted and polished to obtain cross-sectional shape of the weld pool.
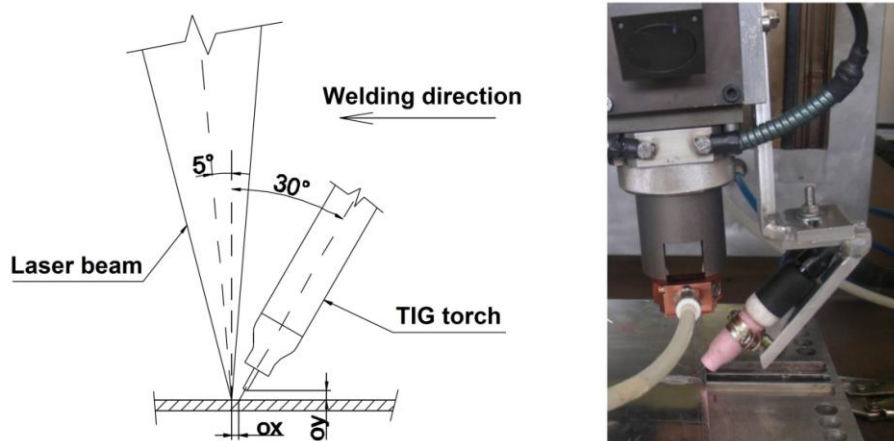
Fig. 19. Experimental set-up of hybrid laser-TIG welding process.

Comparison between simulated and experimental transverse weld pool cross sections are shown in Figs. 20 and 21. Difference percentages between simulated and experimental weld pool depth and half width are respectively 3.4% and 7.3% in fig. 20, and 4.5% and 6.6% in fig. 21. The low values of these difference percentages, as well as, the appropriate match between the simulated and experimental overall shape of the weld pool show that there is a good agreement between simulation and experiment. Accordingly, it can prove the capability of presented numerical model to simulate the weld pool shape and dimensions in hybrid welding process.
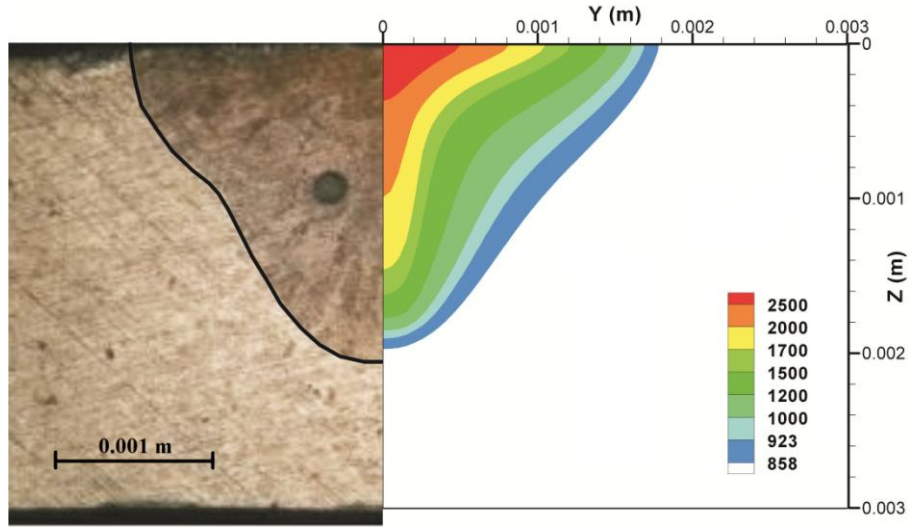
Fig. 20. Comparison between simulated and experimental cross-section of weld pool in hybrid welding at laser power of 2000 W, arc welding current of 100 A and welding speed of 2 m/min.
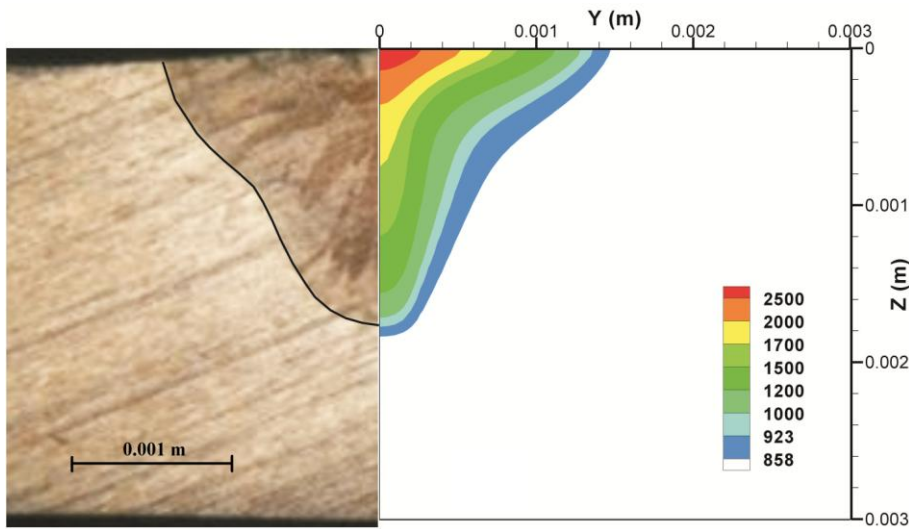
Fig. 21. Comparison between simulated and experimental cross-section of weld pool in hybrid welding at laser power of 2000 W, arc welding current of 100 A and welding speed of 3 m/min.

4. Conclusions

This paper presents a three-dimensional heat transfer and fluid flow model for hybrid laser-TIG welding process. An appropriate model to calculate the current density, magnetic field and electromagnetic (Lorentz) force in the weld pool was proposed by adding four differential equations. In addition, a turbulence model based on Prandtl's mixing length hypothesis was used. A combined effective model consisting of two parts was proposed for laser heat source model. Subsequently, the welding properties such as temperature field and velocity profile in the weld pool were calculated to determine the weld pool shape for welding of aluminum alloy AA6082. Based on performed numerical analysis, the main conclusions can be drawn as follows:

- The electromagnetic model used in this study could offer an appropriate tool to calculate the distribution of current density, magnetic field, and electromagnetic force in the workpiece.

- Since the arc is constricted in hybrid welding process due to the interaction between the arc and laser, a lower effective arc radius was used in hybrid welding than lone TIG welding. This fact results in a slight increase in weld penetration depth in hybrid welding compared to lone laser welding.

- The hybrid welding process leads to a similar weld pool depth, but a wider weld width compared to lone laser welding process, which is caused by higher heat input due to the addition of a TIG heat source in hybrid welding.

- Since the Peclet number was much more than one, the heat in the weld pool is mainly transferred by convection compared to the conduction. Furthermore, the calculated weld pool shape at the presence of convection was in better agreement with the experiment. It means that taking into account heat transfer by convection in the weld pool model is critical to predict the weld pool shape accurately.

- The role of various driving forces for the fluid flow was examined by using several dimensionless numbers. It was found that the liquid metal is driven mainly by the electromagnetic force and the Marangoni stress and, to a much less extent, by buoyancy force. Besides, outward fluid flow at top surface and also clockwise circulation of molten material in upper part of the weld pool can prove the dominancy of the Marangoni force in formation of the weld pool.

- Marangoni convection is stronger in case of hybrid welding than laser or TIG welding, which is possibly originated from the higher amount of molten material and higher temperature gradient experienced in the weld pool.

Hybrid welding process involves many process parameters that should be adjusted appropriately to achieve a high quality weld. However, even if some preliminary experimental tests are needed to adjust the model parameters, this numerical model may be advantageously used to simulate the welding process for large ranges of the welding parameters and their combinations. Therefore, this results in a marked reduction of needed experiments for welding optimization, which causes time and money saving. Hence, future works will be carried out, from both simulation and experimental point of view, to better understand how the welding parameters affect weld pool characteristics and shape in hybrid laser-TIG welding process.

Acknowledgement

References:

1. Bagger C, Olsen FO (2005) Review of laser hybrid welding. Journal of Laser Applications 17 (1):2-14. doi:doi:http://dx.doi.org/10.2351/1.1848532

2. Mahrle A, Beyer E (2006) Hybrid laser beam welding—Classification, characteristics, and applications. Journal of Laser Applications 18 (3):169-180. doi:doi:http://dx.doi.org/10.2351/1.2227012

3. Ribic B, Rai R, DebRoy T (2008) Numerical simulation of heat transfer and fluid flow in GTA/Laser hybrid welding. Science and Technology of Welding and Joining 13 (8):683-693. doi:10.1179/136217108x356782

4. Ribic B, Palmer TA, DebRoy T (2009) Problems and issues in laser-arc hybrid welding. International Materials Reviews 54 (4):223-244. doi:10.1179/174328009x411163

5. Gao M, Zeng X, Hu Q, Yan J (2009) Laser-TIG hybrid welding of ultra-fine grained steel. Journal of Materials Processing Technology 209 (2):785-791. doi:http://dx.doi.org/10.1016/j.jmatprotec.2008.02.062

6. Casalino G, Campanelli SL, Dal Maso U, Ludovico AD (2013) Arc Leading Versus Laser Leading in the Hybrid Welding of Aluminium Alloy Using a Fiber Laser. Procedia CIRP 12 (0):151-156. doi:http://dx.doi.org/10.1016/j.procir.2013.09.027

7. Möller F, Thomy C (2013) Interaction Effects between Laser Beam and Plasma Arc in Hybrid Welding of Aluminum. Physics Procedia 41 (0):81-89. doi:http://dx.doi.org/10.1016/j.phpro.2013.03.054

8. Maletta C, Falvo A, Furgiuele F, Barbieri G, Brandizzi M (2009) Fracture Behaviour of Nickel-Titanium Laser Welded Joints. J of Materi Eng and Perform 18 (5-6):569-574. doi:10.1007/s11665-009-9351-8

9. Rai R, Elmer JW, Palmer TA, DebRoy T (2007) Heat transfer and fluid flow during keyhole mode laser welding of tantalum, Ti–6Al–4V, 304L stainless steel and vanadium. Journal of Physics D: Applied Physics 40 (18):5753–5766

10. Chen YB, Lei ZL, Li LQ, Wu L (2006) Experimental study on welding characteristics of CO2 laser TIG hybrid welding process. Science and Technology of Welding and Joining 11 (4):403-411. doi:doi:10.1179/174329306X129535

11. Faraji AH, Bahmani A, Goodarzi M, Seyedein SH, Shbani MO (2014) Numerical and experimental investigations of weld pool geometry in GTA welding of pure aluminum. J Cent South Univ 21:20-26. doi:10.1007/s11771-014-1910-y

12. Faraji A, Goodarzi M, Seyedein S, Zamani M (2014) Experimental study and numerical modeling of arc and weld pool in stationary GTA welding of pure aluminum. Int J Adv Manuf Technol:1-13. doi:10.1007/s00170-014-5651-8

13. Dong W, Lu S, Li D, Li Y (2011) GTAW liquid pool convections and the weld shape variations under helium gas shielding. International Journal of Heat and Mass Transfer 54 (7–8):1420-1431. doi:http://dx.doi.org/10.1016/j.ijheatmasstransfer.2010.07.069

14. Traidia A, Roger F (2011) Numerical and experimental study of arc and weld pool behaviour for pulsed current GTA welding. International Journal of Heat and Mass Transfer 54 (9–10):2163-2179. doi:http://dx.doi.org/10.1016/j.ijheatmasstransfer.2010.12.005

15. Dong W, Lu S, Li D, Li Y (2010) Modeling of the Weld Shape Development During the Autogenous Welding Process by Coupling Welding Arc with Weld Pool. J of Materi Eng and Perform 19 (7):942-950. doi:10.1007/s11665-009-9570-z

16. Zhang W, Kim CH, DebRoy T (2004) Heat and fluid flow in complex joints during gas metal arc welding-Part II: Application to fillet welding of mild steel. Journal of Applied Physics 95 (9):5220-5229. doi:10.1063/1.1699486

17. Goodarzi M, Choo R, Takasu T, Toguri JM (1998) The effect of the cathode tip angle on the gas tungsten arc welding arc and weld pool: II. The mathematical model for the weld pool. Journal of Physics D: Applied Physics 31 (5):569-583

18. Rai R, Kelly SM, Martukanitz RP, DebRoy T (2008) A Convective Heat-Transfer Model for Partial and Full Penetration Keyhole Mode Laser Welding of a Structural Steel. Metall and Mat Trans A 39 (1):98-112. doi:10.1007/s11661-007-9400-6

19. Rai R, Roy GG, DebRoy T (2007) A computationally efficient model of convective heat transfer and solidification characteristics during keyhole mode laser welding. Journal of Applied Physics 101 (5). doi:doi:http://dx.doi.org/10.1063/1.2537587

20. Moradi M, Ghoreishi M, Frostevarg J, Kaplan AFH (2013) An investigation on stability of laser hybrid arc welding. Optics and Lasers in Engineering 51 (4):481-487. doi:http://dx.doi.org/10.1016/j.optlaseng.2012.10.016

21. Brandizzi M, Satriano AA, Sorgente D, Tricarico L (2013) Laser–arc hybrid welding of Ti6Al4V titanium alloy: mechanical characterization of joints and gap tolerance. Welding International 27 (2):113-120. doi:10.1080/09507116.2011.600045

22. Tani G, Campana G, Fortunato A, Ascari A (2007) The influence of shielding gas in hybrid LASER–MIG welding. Applied Surface Science 253 (19):8050-8053. doi:http://dx.doi.org/10.1016/j.apsusc.2007.02.144

23. Piekarska W, Kubiak M (2011) Three-dimensional model for numerical analysis of thermal phenomena in laser–arc hybrid welding process. International Journal of Heat and Mass Transfer 54 (23–24):4966-4974. doi:http://dx.doi.org/10.1016/j.ijheatmasstransfer.2011.07.010

24. Piekarska W, Kubiak M (2013) Modeling of thermal phenomena in single laser beam and laser-arc hybrid welding processes using projection method. Applied Mathematical Modelling 37 (4):2051-2062. doi:http://dx.doi.org/10.1016/j.apm.2012.04.052

25. Kong F, Ma J, Kovacevic R (2011) Numerical and experimental study of thermally induced residual stress in the hybrid laser–GMA welding process. Journal of Materials Processing Technology 211 (6):1102-1111. doi:http://dx.doi.org/10.1016/j.jmatprotec.2011.01.012

26. Kong F, Kovacevic R (2010) 3D finite element modeling of the thermally induced residual stress in the hybrid laser/arc welding of lap joint. Journal of Materials Processing Technology 210 (6–7):941-950. doi:http://dx.doi.org/10.1016/j.jmatprotec.2010.02.006

27. Gao Z, Ojo OA (2012) Modeling analysis of hybrid laser-arc welding of single-crystal nickel-base superalloys. Acta Materialia 60 (6–7):3153-3167. doi:http://dx.doi.org/10.1016/j.actamat.2012.02.021

28. Xu GX, Wu C, Qin GL, Wang XY, Lin SY (2011) Adaptive volumetric heat source models for laser beam and laser + pulsed GMAW hybrid welding processes. Int J Adv Manuf Technol 57 (1-4):245-255. doi:10.1007/s00170-011-3274-x

29. Le Guen E, Carin M, Fabbro R, Coste F, Le Masson P (2011) 3D heat transfer model of hybrid laser Nd:Yag-MAG welding of S355 steel and experimental validation. International Journal of Heat and Mass Transfer 54 (7–8):1313-1322. doi:http://dx.doi.org/10.1016/j.ijheatmasstransfer.2010.12.010

30. Zhou J, Tsai HL (2008) Modeling of transport phenomena in hybrid laser-MIG keyhole welding. International Journal of Heat and Mass Transfer 51 (17–18):4353-4366. doi:http://dx.doi.org/10.1016/j.ijheatmasstransfer.2008.02.011

31. Xu P-q, Bao C-m, Lu F-g, Ma C-w, He J-p, Cui H-c, Yang S-l (2011) Numerical simulation of laser–tungsten inert arc deep penetration welding between WC–Co cemented carbide and invar alloys. Int J Adv Manuf Technol 53 (9-12):1049-1062. doi:10.1007/s00170-010-2898-6

32. Abderrazak K, Bannour S, Mhiri H, Lepalec G, Autric M (2009) Numerical and experimental study of molten pool formation during continuous laser welding of AZ91 magnesium alloy. Computational Materials Science 44 (3):858-866. doi:http://dx.doi.org/10.1016/j.commatsci.2008.06.002

33. Patankar SV (1980) Numerical Heat Transfer and Fluid Flow. McGraw-Hill, New York

34. Roy GG, Elmer JW, DebRoy T (2006) Mathematical modeling of heat transfer, fluid flow, and solidification during linear welding with a pulsed laser beam. Journal of Applied Physics 100 (3). doi:doi:http://dx.doi.org/10.1063/1.2214392

35. He X, Elmer JW, DebRoy T (2005) Heat transfer and fluid flow in laser microwelding. Journal of Applied Physics 97 (8). doi:doi:http://dx.doi.org/10.1063/1.1873032

36. Zhang W, Kim C-H, DebRoy T (2004) Heat and fluid flow in complex joints during gas metal arc welding—Part I: Numerical model of fillet welding. Journal of Applied Physics 95 (9):5210-5219. doi:doi:http://dx.doi.org/10.1063/1.1699485

37. Lago F, Gonzalez JJ, Freton P, Gleizes A (2004) A numerical modelling of an electric arc and its interaction with the anode: Part I. The two-dimensional model. JOURNAL OF PHYSICS D: APPLIED PHYSICS 37 (6):883-897

38. Lu F, Yao S, Lou S, Li Y (2004) Modeling and finite element analysis on GTAW arc and weld pool. Computational Materials Science 29 (3):371-378. doi:http://dx.doi.org/10.1016/j.commatsci.2003.10.009

39. Gonzalez JJ, Lago F, Freton P, Masquère M, Franceries X (2005) Numerical modelling of an electric arc and its interaction with the anode: part II. The three-dimensional model—influence of external forces on the arc column. Journal of Physics D: Applied Physics 38 (2):306-318

40. Jamshidi Aval H, Farzadi A, Serajzadeh S, Kokabi AH (2009) Theoretical and experimental study of microstructures and weld pool geometry during GTAW of 304 stainless steel. Int J Adv Manuf Technol 42 (11-12):1043-1051. doi:10.1007/s00170-008-1663-6

41. Farzadi A, Serajzadeh S, Kokabi AH (2010) Investigation of weld pool in aluminum alloys: Geometry and solidification microstructure. International Journal of Thermal Sciences 49 (5):809-819. doi:http://dx.doi.org/10.1016/j.ijthermalsci.2009.11.007

42. Cantin GMD, Francis JA (2005) Arc power and efficiency in gas tungsten arc welding of aluminium. Science and Technology of Welding and Joining 10 (2):200-210. doi:doi:10.1179/174329305X37033

43. Tsai NS, Eagar TW (1985) Distribution of the heat and current fluxes in gas tungsten arcs. MTB 16 (4):841-846. doi:10.1007/bf02667521

44. Wu CS, Gao JQ (2002) Analysis of the heat flux distribution at the anode of a TIG welding arc. Computational Materials Science 24 (3):323-327. doi:http://dx.doi.org/10.1016/S0927-0256(01)00254-3

45. Haiyan Z, Wenchong N, Bin Z, Yongping L, Masaru K, Takashi I (2011) Modelling of keyhole dynamics and porosity formation considering the adaptive keyhole shape and three-phase coupling during deep-penetration laser welding. Journal of Physics D: Applied Physics 44 (48):485302

46. Farzadi A, Serajzadeh S, Kokabi AH (2008) Modeling of heat transfer and fluid flow during gas tungsten arc welding of commercial pure aluminum. Int J Adv Manuf Technol 38 (3-4):258-267. doi:10.1007/s00170-007-1106-9